Bulletin of the Seismological Society of America, Vol. 97, No. 2, pp. 426–439, April 2007, doi: 10.1785/0120060113

Correlation of *Lg* Amplitude Ratios from Peaceful Nuclear Explosions to Crustal Structure in Northern Eurasia

by Hongyan Li,* Igor B. Morozov, and Scott B. Smithson

Abstract Because the *Lg* phase is strongly affected by the variations of crustal structure in some areas, understanding these factors is important for nuclear test monitoring. This study examines the effects of regional tectonic structure on *Lg* propagation by using the Peaceful Nuclear Explosion (PNE) profiles in Russia. The logarithms of *Lg*/*Sn* and *Lg*/*Pcoda* PNE-amplitude ratios within the 0.5- to 3-Hz frequency band are measured and correlated with the regional crustal structures. Both ratios are found to decrease within the areas with thick, low-velocity sedimentary cover and across tectonic boundaries with abrupt variations of crustal thickness. For the offset derivatives of both the logarithmic ratios, a linear relationship to the slopes of the Moho and the vertical travel times within the sedimentary cover is determined. A strong negative slope is observed along both crustal thinning and crustal thickening segments, and a positive slope follows the negative slope across a crustal thickening segment. Therefore, crustal thinning appears to affect the *Lg* propagation stronger than crustal thickening, which could be due to focusing *Lg* energy within the crustal wave guide. The log-amplitude regression provided in this article could be useful for predicting *Lg* behavior in areas where amplitude measurements are not available.

Introduction

Because the *Lg* phase is strongly affected by the variations of crustal structure in some areas, understanding these factors is important for nuclear test monitoring. The *Lg* phase is interpreted as consisting of multiple supercritical *S*-wave reflections or a superposition of higher-mode surface waves trapped within the crust (Knopoff *et al.*, 1973; Campillo, 1987). For nuclear explosions, near-source scattering of *Rg* into *S* is a primary contributor to the low-frequency *Lg* (Gupta *et al.*, 1992, 1997; He *et al.*, 2005).

The *Lg*-phase amplitudes measured within selected frequency bands are often used to describe *Lg*-propagation characteristics in different tectonic areas. Rapine and Ni (2003) compared the *Lg* amplitude and prephase noise to measure the efficiency of *Lg* propagation. Several phase-amplitude ratios: *Pg*/*Lg* (Phillips *et al.*, 2001) or *Lg*/*Pg* (Sandvol *et al.*, 2001), and *Lg*/*Pcoda* (Rapine *et al.*, 1997; McNamara and Walter, 2001) were used to calibrate *Lg*-phase propagation across different crustal structure. In most studies (Rapine *et al.*, 1997; Baumgardt, 2001; McNamara and Walter, 2001; Phillips *et al.*, 2001; Sandvol *et al.*, 2001; Rapine and Ni, 2003), the *Lg*-propagation characteristics were derived from earthquake data. Because these data typically have relatively sparse coverage and the stations are rarely deployed in-line with the sources, such approaches provide general characterizations of the area, yet do not allow us to study the detailed evolution of *Lg*-phase amplitude during its propagation away from the source and across geological and tectonic boundaries. In addition, an *Lg* generated from a nuclear-bomb source is, of course, ideal for test calibration.

Fortunately for seismic calibration of propagation in northern Eurasia and despite the paucity of its natural seismicity, extensive and unusually detailed recordings of short-period *Lg* and other regional phases are available in this region. From the 1970s and to late the 1980s, Russian scientists acquired a network of dense, linear, 2000- to 4000-km-long, three-component deep seismic sounding (DSS) profiles using chemical and Peaceful Nuclear Explosions (PNEs) with nearly coincident recording. Seven of these profiles including 19 PNEs were used in this study (Fig. 1). These long-offset, dense, three-component seismic records with known locations and propagation times allow measurement of *Lg*-phase propagation parameters at 10- to 15-km station spacing in one of the largest landmasses on Earth to test the available models and relate these parameters to crustal structure. Many of these segments of profiles are reversed, which provides even more unique data to analyze.

By comparing the logarithms of amplitude ratios of the *Lg* phase over *Pn, Pg, Sn, Pcoda*, and prephase noise (Fig. 2) within different frequency bands, the present study

---

*Present address: 10053 Westpark Drive, #296, Houston, Texas 77042, lhysnow@yahoo.com.

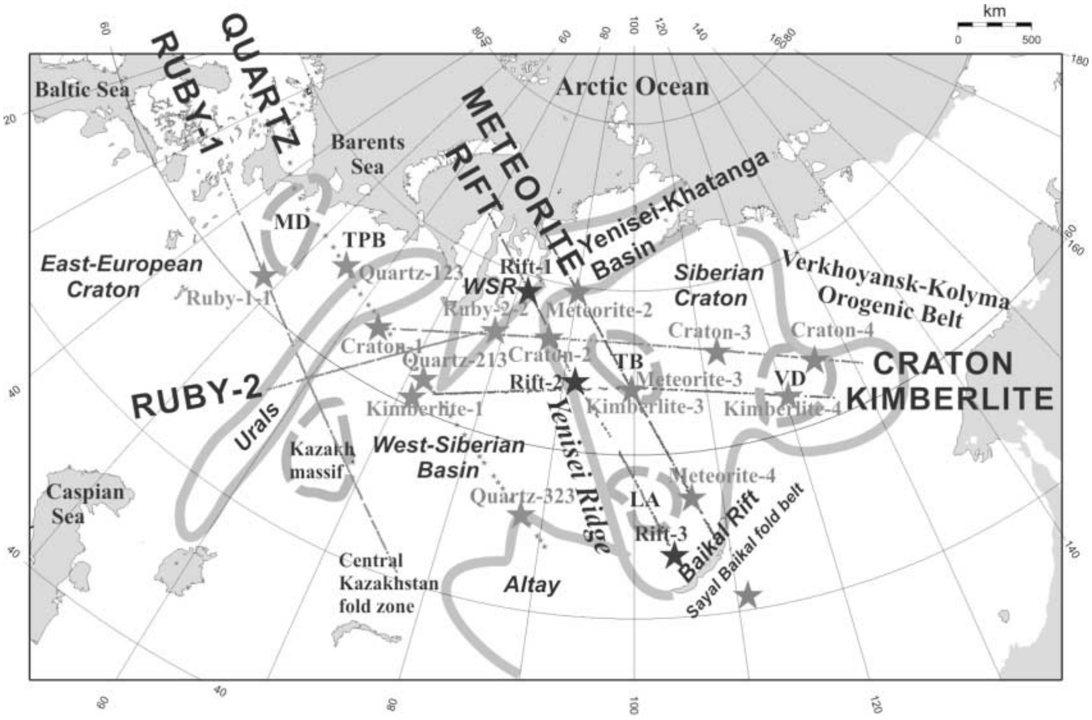

Figure 1. Location of PNE profiles and tectonic boundaries in northern Eurasia. Large stars are the PNE locations. Thick solid lines show major tectonic features (WSR, West Siberian Rift; MD, Mezen Depression; TPB, Timan-Pechora Basin; Zonenshain *et al.*, 1990). The three major basins within the Siberian Craton are Tunguss Basin (TB), Vilyui Depression (VD), and Low Angara Basin (LA).

uses $\log(A_{Lg}/A_{Sn})$ and $\log(A_{Lg}/A_{Pcoda})$ to correlate the slopes of the logarithm of amplitude ratios with the variations of crustal structure and to determine the main factors affecting *Lg* propagation. From the observations of the variations of the slopes in different tectonic areas, a two-parameter linear regression model is proposed to calibrate the variations of *Lg* amplitude. The resulting two parameters that appear to describe the observed correlations best are the Moho slope and the vertical *S*-wave travel time within the sedimentary basins. From the strongest anomalies in the slopes of the log-amplitude ratios, the main tectonic areas affecting *Lg* propagation in northern Eurasia were identified. These areas are the Vilyui Depression, Ural Mountains, Yenisei Ridge (the boundary between the West Siberian Basin and the Siberian Craton), the boundary between the Kazakh massif and the West Siberian Basin, the Mezen depression, the West Siberian Rift, and the West Siberian Basin.

Geological and Tectonic Setting

A variety of contrasting geological structures are present in the vast geographical expanse of northern Eurasia (Fig. 1), and thus the seismic profiles crossing the different tectonic provinces provide a good database to calibrate the effects of crustal structure on regional phase propagation. The seven PNE profiles of this study (QUARTZ, RUBY-1, RUBY-2, CRATON, KIMBERLITE, RIFT, and METEORITE) mainly traverse (listed from west to east, Fig. 1): the East European Craton, Timan fold belt and Timan-Pechora Basin, Uralian fold belt, West Siberian Basin, West Siberian Rift (Pur-Gurden Basin), Altay-Sayan-Baikal folded region, Siberian Craton, and Baikal Rift Zone.

The crustal thickness of the East European Craton is 36–48 km, and the surrounding areas have generally thinner crust than its inner part (Volkov, 1984; Pavlenkova, 1996). The northern part of the East European Craton includes the stable Baltic Shield, which lacks significant sedimentary cover (Gaal and Gorbatschev, 1987). Between the eastern margin of the Baltic Shield and the Timan belt, the basement is disrupted by narrow and deep (in excess of 3 km) graben-like troughs called aulacogens or failed rifts (Zonenshain *et al.*, 1990).

The Timan-Pechora platform (Fig. 1) is mainly composed of the Timan-Pechora fold belt and Timan-Pechora Basin. The crustal thickness in this area is 36–40 km (Pavlenkova, 1996), and the sedimentary cover in the southern plain averages 3–7 km (Zonenshain *et al.*, 1990) with average velocity of ~4.2 km/sec (Beloussov *et al.*, 1992a, b).

The Uralian fold belt (Fig. 1) represents a linear collisional fold belt formed at the end of the Paleozoic and the very beginning of the Mesozoic (310–220 Ma) (Zonenshain *et al.*, 1990). The crustal thickness is about 40–53 km, with

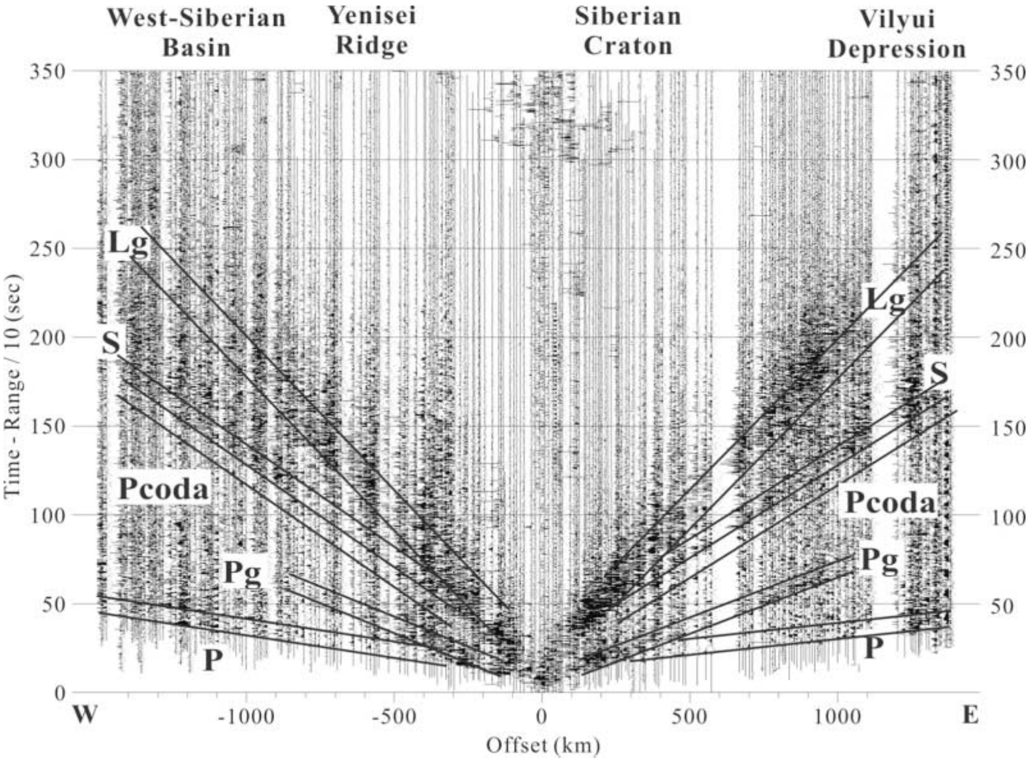

Figure 2. Seismic record of PNE Kimberlite-3, filtered within a frequency band 0.5–8 Hz. The regional phases (*Pn, Pg, Sn*, and *Lg*) are clear and are observed to far offsets. *Lg* in the western branch is significantly weaker than in the eastern one. Within the eastern branch, *Lg* becomes weak within the Vilyui Depression. The solid lines show the time window of *Pn, Pg, Pcoda, Sn*, and *Lg* used for computing amplitude ratios.

a ~14-km crustal root (Carbonell *et al.*, 1996; Pavlenkova, 1996; Morozova *et al.*, 1999; Tryggvason *et al.*, 2001).

The basement of the West Siberian Basin (Fig. 1) was formed of Paleozoic fold structures of various ages and older Precambrian blocks (Zonenshain *et al.*, 1990) with subsidence from Triassic to Neogene (Khain, 1994). The subsidence was accompanied by extensive basaltic volcanism, which was also confirmed by drilling (Saunders *et al.*, 2005). The basin is mainly covered by Mesozoic and Cenozoic sediments (Aplonov, 1995) with velocities of 2.5–5 km/sec, averaging ~10 km in thickness in the north and ~3 km in the south (Aplonov, 1995; Ulmishek, 2003). The crustal thickness decreases from the edges (~42 km) to the central part of the platform (~34 km in the north along the West Siberian Rift; Aplonov, 1995). The Kazakh massif is located southwest of the West Siberian Basin and has a thick crust (40–45 km) with high average velocities (6.6–6.8 km/sec), comparable to those of the Baltic shield (Pavlenkova, 1996). The sedimentary cover in the Kazakh massif is less than 2 km.

The western part of the Siberian Craton, in general, is covered by a 5- to 6-km-thick sedimentary cover containing from 100–150- to 1400-m-thick flood basalts of the Mesozoic Siberian Traps (Czamanske *et al.*, 1998; Pavlenkova *et al.*, 2002). Within the Tunguss and Low Angara Basins, the sedimentary cover is up to 10 km (Egorkin *et al.*, 1987; Pavlenkova, 1996; Pavlenkova *et al.*, 2002). The Tunguss Basin is filled with a high-velocity (4.5–6.0 km/sec) Devonian sedimentary cover with a relatively flat Moho (~50 km) in the north (Egorkin *et al.*, 1987; Pavlenkova, 1996), but a Moho uplift (~3 km) in the south (Pavlenkova, 1996; GEON, personal communication). The Low Angara Basin is filled with both Paleozoic and Mesozoic sedimentary cover with somewhat lower velocities (3.5–6 km/sec), and the basement subsidence is compensated by a ~3- to 4-km Moho uplift (Pavlenkova, 1996). The Vilyui Depression is filled with 10–14 km of loose and low-velocity Mesozoic rocks (2.5–4.5 km/sec), and the basement surface has steep dips with an up to 13-km antiroot in the Moho (Egorkin *et al.*, 1987; Pavlenkova, 1996). The crustal thickness is 40–45 km on the average (Pavlenkova, 1996) increasing to 50 km below the Tunguss Basin and decreasing to ~35 km below the Vilyui Depression (Egorkin *et al.*, 1987; Pavlenkova, 1996; Pavlenkova *et al.*, 2002).

The Altay Mountains and Sayan-Baikal fold belt (Fig. 1) are composed of several different units assembled by accretion of island arcs, in general, in the Late Precambrian and Paleozoic (Volkov, 1984; Khain, 1985). Under the Altai Mountains, the crust could be thicker than 50 km and even reach 60 km (Pavlenkova, 1996; Morozova *et al.*, 1999; Dehandschutter, 2001). The crustal thickness beneath the Sayan-Baikal fold belt ranges from 36 to 55 km while remaining between 40 and 45 km in most parts of the area (Beloussov *et al.*, 1992a, b).

The West Siberian Rift (Pur-Gurden Basin; Fig. 1) is located on the northwest edge of the Siberian platform, a failed ocean of rift origin developed in the Triassic during the initial breakup of Pangea. Since the cessation of extension, the West Siberian Rift was filled by up to 13-km-thick sediments (Cipar *et al.*, 1993; Aplonov, 1995).

The Baikal Rift zone (BRZ; Fig. 1) is seismically active, still rifting, and represents one of the deepest rifts on Earth (Golmshtok *et al.*, 2000). The Late Cenozoic sediments are usually 2.5–3 km thick and even reach up to 7 km in thickness within the rift basins (Logatchev and Zorin, 1992; Hutchinson *et al.*, 1992). The heat flow in the Baikal Rift is 60–75 mW/m^2, which is much lower than in other continental rifts (usually $>$100 mW/m^2). The thickness of the crust beneath the Baikal Rift Zone was inferred to be 35–45 km (Dehandschutter, 2001). Below the Moho, a layer of low mantle velocities (7.7–7.8 km/sec, 0.3–0.5 km/sec lower than in the adjoining areas) was identified, pinching out toward the Siberian Craton (Beloussov *et al.*, 1992a, b; Zorin *et al.*, 2003), which could be related to the relatively high-heat flow.

Data Analysis

Data Selection

Because of the limited data length of some traces in the PNE records, a constant window length was used to measure the amplitude of all the phases for amplitude ratios (*Lg*/*Pn, Lg*/*Pg, Lg*/*Sn*, and *Lg*/P_{coda}). The phases were identified by correlating the record sections (Fig. 2), and their onset times were picked interactively. The *Lg* and *Sn* phases could usually be distinguished beyond offsets of ~300 km (Fig. 2), and therefore, the amplitude ratios were computed at offsets exceeding that distance. The observed durations of the *Pn, Pg*, and *Sn* wave trains were typically 10 to 20 sec, whereas the duration of *Lg* was longer, usually $>$20 sec (Fig. 2). Therefore, the phase-window length was chosen to equal 10 sec for the *Pn, Sn*, and *Pg* waves and 20 sec for the *Lg*. The window of the *P*-wave coda, referred to as *Pcoda*, was taken to be 10 sec immediately preceding the *Sn*-wave onset times. For the *Pn*-wave window, if the interval between its onset and the *Pg* was less than 10 sec, the window was truncated at the picked onset of the *Pg* phase. For the *Sn*-wave window, if the interval between its onset and the *Lg* was less than 10 sec, the window was truncated at the picked onset of the *Lg* phase. The time windows were checked for spikes, data dropouts, and clipped amplitudes, and the amplitude ratios were computed with only the good traces.

As an example of a PNE seismic section, Figure 2 shows a record from PNE Kimberlite-3 detonated within the western part of the Siberian Craton. All the regional phases (*Pn, Pg, Sn*, and *Lg*) are strong in the regional offset range. The *Pn* and *Sn* are strong at far offsets ($>$1000 km) in both directions. The western branch of *Lg*, which travels into the West Siberian Basin, is significantly weaker than the eastern one, traveling within the Siberian Craton. The *Lg* becomes very weak at ~1100 km offsets from the shot point, where it enters the Vilyui Depression. Similarly to the *Lg*, the *Pg* is visible to ~−700 km to the west and ~1000 km to the east, where it appears to become quickly attenuated within the Vilyui Depression.

A Model for the Logarithm of Amplitude Ratios

To describe the empirical distance dependence of the *Lg*-phase amplitude at offsets x_1 and x_2 (A_{Lg1} and A_{Lg2}, respectively) within a given frequency band, we use the geometrical spreading and attenuation relation:

$$A_{Lg2} = A_{Lg1}\left(\frac{x_2}{x_1}\right)^{-\gamma_{Lg}} e^{-\eta_{Lg}(x_2-x_1)}, \qquad (1)$$

where γ_{Lg} is geometrical spreading parameter of *Lg* and η_{Lg} is the average attenuation factor of *Lg* between offsets x_1 and x_2. Similarly, for the body-wave phases:

$$A_{Ph2} = A_{Ph1}\left(\frac{x_2}{x_1}\right)^{-\gamma_{Ph}} e^{-\eta_{Ph}(x_2-x_1)}, \qquad (2)$$

where *Ph* represents the *Pn* or *Sn* phase, A_{Ph1} and A_{Ph2} are the corresponding amplitudes at x_1 and x_2, respectively, γ_{Ph} is the geometrical spreading parameter, and η_{Ph} is the attenuation factor between x_1 and x_2.

By taking the logarithm of the ratio of the amplitudes in equations (1) and (2), we obtain:

$$\log\left(\frac{A_{Lg2}}{A_{Ph2}}\right) - \log\left(\frac{A_{Lg1}}{A_{Ph1}}\right) = (\gamma_{Ph} - \gamma_{Lg})(\log(x_2) - \log(x_1)) + (\eta_{Ph} - \eta_{Lg})(x_2 - x_1). \qquad (3)$$

Therefore, the difference of $\log(A_{Lg}/A_{Ph})$ between distances x_1 and x_2 is the differences of geometrical spreading and attenuation of the two phases between distances x_1 and x_2.

Although a controversy can be noted in their interpretation (Ryberg *et al.*, 1995; Morozov, 2001; Nielsen and Thybo, 2003), codas of the “fast” PNE phase (regional to teleseismic *Pn*) propagating through the upper mantle were interpreted as scattering the wave field in the crust, especially the heterogeneous lower crust (Nielsen and Thybo, 2003). These coda waves sample large areas around the receivers, and they should be less affected by the variations of the crustal structure than *Pg* and *Lg* phases (Morozov *et al.*, 2002). Therefore, the *Lg*/*Pcoda* amplitude ratios could be expected to be a more stable parameter to measure the effects of the variations of crustal structure on *Lg* propagation.

For *Pcoda* immediately before the *Sn*-wave onset at distances x_1 and x_2:

$$A_{Pcoda1} = A_{P1}(t_1 - t_{01})^{-\gamma_{Pcoda}} e^{-\omega(t_1 - t_{01})/Q_c} = A_{P1}\left(\frac{x_1}{V_S} - t_{Pcoda} - \frac{x_1}{V_P}\right)^{-\gamma_{Pcoda}} e^{-\omega(x_1/V_S - t_{Pcoda} - x_1/V_P)/Q_c}, \quad (4)$$

$$A_{Pcoda2} = A_{P2}\left(\frac{x_2}{V_S} - t_{Pcoda} - \frac{x_2}{V_P}\right)^{-\gamma_{Pcoda}} e^{-\omega(x_2/V_S - t_{Pcoda} - x_2/V_P)/Q_c}, \quad (5)$$

where A_{Pcoda1} and A_{Pcoda2} are *Pcoda* amplitudes at distances x_1 and x_2 before the *Sn* phase; A_{P1} and A_{P2} are *Pn*-phase amplitudes at distances x_1 and x_2; γ_{Pcoda} is the geometrical spreading parameter of *Pcoda* and η_{Pcoda} is the attenuation parameter of *Pcoda*; ω is the angular frequency; V_p and V_s are *Pn*- and *Sn*-phase velocities, respectively; t_1 and t_{01} are the start time of *Pcoda* and *Pn* phase at distance x_1, and t_2 and t_{02} are the start time of *Pcoda* and *Pn* phase at distance x_2.

Because the time length of *Pcoda* (t_{Pcoda}, taken as 10 sec in this study) is small compared with the start times of the *Sn* phase at far offsets:

$$\frac{x_1}{V_s} - t_{Pcoda} \approx \frac{x_1}{V_s},$$

and therefore,

$$A_{Pcoda1} \approx A_{P1}\left(\frac{x_1}{V_S} - \frac{x_1}{V_P}\right)^{-\gamma_{Pcoda}} e^{-\eta_{Pcoda}x_1} \quad (6)$$

$$A_{Pcoda2} \approx A_{P2}\left(\frac{x_2}{V_S} - \frac{x_2}{V_P}\right)^{-\gamma_{Pcoda}} e^{-\eta_{Pcoda}x_2}. \quad (7)$$

According to equation (2),

$$A_{Pcoda2} = A_{P1}\left(\frac{x_2}{x_1}\right)^{-\gamma_P} e^{-\eta_P(x_2 - x_1)}\left(\frac{x_2}{V_S} - \frac{x_2}{V_P}\right)^{-\gamma_{Pcoda}} e^{-\eta_{Pcoda}x_2}. \quad (8)$$

From equations (1), (6), and (8),

$$\log\left(\frac{A_{Lg2}}{A_{Pcoda2}}\right) - \log\left(\frac{A_{Lg1}}{A_{Pcoda1}}\right) = (\gamma_P + \gamma_{Pcoda} - \gamma_{Lg})(\log(x_2) - \log(x_1)) + (\eta_P + \eta_{Pcoda} - \eta_{Lg})(x_2 - x_1). \quad (9)$$

Therefore, the difference of $\log(A_{Lg}/A_{Pcoda})$ between distances x_1 and x_2 is the difference of geometrical spreading of *Pn* and *Pcoda* with *Lg* and the difference in attenuation of *Pn* and *Pcoda* with *Lg* between distances x_1 and x_2.

Selection of Calibration Parameters

In interpreting equations (3) and (9), our fundamental assumption is that the geometrical spreading parameters (γ) and most likely η_P, η_S, and η_{Coda} are relatively smoothly varying with offsets (x), whereas crustal attenuation parameter η_{Lg} should be most sensitive to crustal heterogeneity. Subtraction of the regional offset trend from the logarithms of the amplitude ratios should thus remove the effects of geometrical spreading and average attenuation, and the residual variations of the log-amplitude ratios should only be mostly due to the attenuation along different crustal paths.

Because of the variability of the *Pn*-wave amplitudes, the scatter in the observed values of $\log(A_{Lg}/A_{Pn})$ is much larger than that of $\log(A_{Lg}/A_{Sn})$ and $\log(A_{Lg}/A_{Pcoda})$, which are similar in magnitudes. Consequently, this article uses the more stable $\log(A_{Lg}/A_{Sn})$ and $\log(A_{Lg}/A_{Pcoda})$ to correlate the variations of amplitude ratios with the crustal structure.

Comparison of the logarithms of amplitude ratios measured within different frequency bands (Fig. 3) shows that both ratios decrease with frequency, indicating that the *Lg*-phase energy is concentrated at lower frequencies than *Sn* and *Pcoda*. Moreover, variations of the log-amplitude ratios at low frequencies correlate with the variations of crustal structure better than those at higher frequencies. At low frequencies, both ratios decrease gently or increase with offset within the Siberian Craton (except in the Vilyui Depression) while they decrease quickly with the travel paths in the Vilyui Depression and the West Siberian Basin (Fig. 3). Therefore, a 0.5- to 3-Hz frequency band was used in this study.

The amplitude ratios were computed by using single-component and vector measures, and also using different methods (root-mean-square [rms], median, and peak values) to compare the stability of these measures. The ratios determined from the first two methods were close, whereas the ratios of peak amplitudes showed large outliers and higher scatter. Vector measures provide consistently more stable estimates, apparently due to partial compensation of the effects of scattering (Kennett, 1993). In the following, we present the amplitude ratios computed using the rms vector measure.

Because the *Pn*- and often *Sn*-wave phases are strong in PNE records, their codas contribute to the amplitudes of the later phases, resulting in amplitude buildup competing with coda decay (Morozov *et al.*, 2002). In this study, we do not attempt to remove the effects of the preceding coda contributions from the *Lg*. Instead, as is commonly done in observational seismology, we simply associate the average (rms) amplitude within the corresponding phase windows. For example, the amplitude measured within the *Lg*-time window as labeled as the *Lg* amplitude, A_{Lg}, and similarly for other phases (Fig. 2).

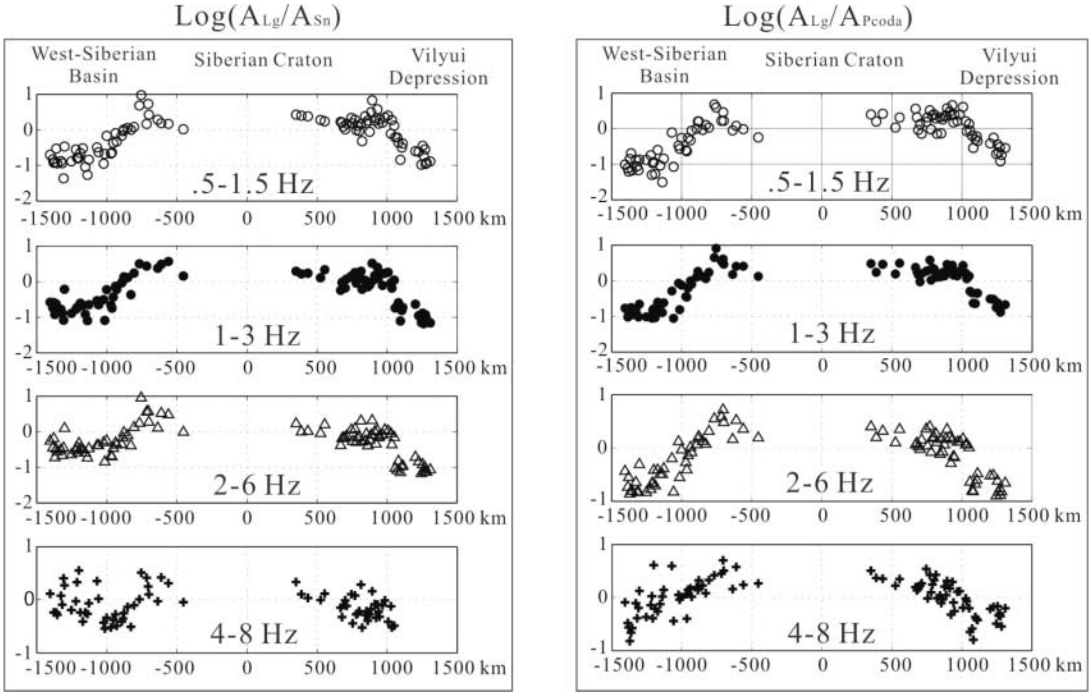

Figure 3. Logarithms of *Lg*/*Sn* and *Lg*/*Pcoda* vector amplitude ratios from PNE Kimberlite-3 along KIMBERLITE profile (Fig. 1) within different frequency bands. The variation range of the amplitude ratios decreases with the increase of frequencies. Both ratios at low frequencies correlate better with the variations of crustal structure; in general, keep constant or increase with offset in the Siberian Craton; and decrease with offset in the West Siberian Basin and the Vilyui Depression.

Correlation of the Amplitude Ratios with Crustal Structure

After removal for the average offset trends, both $\log(A_{Lg}/A_{Sn})$ and $\log(A_{Lg}/A_{Pcoda})$ exhibit local variations that appear to correlate with local structures. Along the CRATON profile (Fig. 4), the slopes of both ratios from the PNEs are $\sim -0.0017 \pm 0.0005$ km^{-1} within the Ob-Tasovsk Depression (profile distances, 0–1000 km). This area is characterized by a thick (~8 km) and low-velocity (V_P 2.5–5 km/sec) sedimentary cover and a rugged Moho (Fig. 4). The slopes of both ratios change to $\sim -0.005 \pm 0.001$ km^{-1} near km ~1000–1200, where the crustal thickness increases by ~10 km from the West Siberian Basin to the Yenisei Ridge. The slopes are small (~0 km^{-1}) from km 1300 to 2500, corresponding to the ~8-km-thick, but high-velocity (V_P 4.5–6 km/sec) Tunguss Basin and the Mirninsk-Aihalsk High with a thin sedimentary cover and small Moho variation (<5 km). The slopes are highly negative (-0.0035 to -0.0045 km^{-1} from Craton-2 and Craton-3 from km 2700 to 3000, -0.005 to -0.007 km^{-1} from Craton-4 from km 2700 to 2500) within the Vilyui Depression corresponding to an abrupt variation of crustal thickness (>10 km) combined with a thick (up to 13 km) low-velocity (V_P ~4 km/sec) sedimentary cover.

At profile distances from km 2300 to 2700, the slopes of both ratios from Craton-2 differ from those of Craton-4 (Fig. 4). For PNE Craton-2, the slope is ~0 until km ~2700 followed by a strong negative slope (-0.004 to -0.0045 km^{-1}) to background level near km ~3000 (Fig. 4). For PNE Craton-4, the slope is ~ -0.005 to -0.007 km^{-1} from km ~2700 to 2500, followed by a positive slope ~0.0024 to 0.004 km^{-1} until km ~2300.

Along RUBY-1 profile, across the Ural Mountains (Fig. 5), the slope is -0.007 to -0.006 km^{-1} corresponding to the up to 14 km crustal root (Carbonell *et al.*, 1996; Pavlenkova, 1996; Morozova *et al.*, 1999; Tryggvason *et al.*, 2001), and a positive slope ~0.003 km^{-1} is also observed at farther offsets.

The amplitude ratios from both the Vilyui Depression and the Ural Mountains show that the effect of the variation of crustal thickness on the variation of amplitude ratios, that is, the slope of the amplitude ratios, depends on the propagation direction. The effect of crustal thickening is different from that of crustal thinning.

Within the West Siberian Basin, the Moho depth is ~40 km with gentle variations, and the sedimentary cover is up to 8 km with velocities of 2.5–5 km/sec. The slopes of both amplitude ratios are determined as ~ -0.0017 km^{-1} (Fig. 4). Within the Tunguss Basin, the Moho depth is ~50 km with gentle variations, and the sedimentary cover is up to 10 km with velocities of 4.5–6.0 km/sec. The slopes of both amplitude ratios are quite flat (~0; Fig. 4). The com-

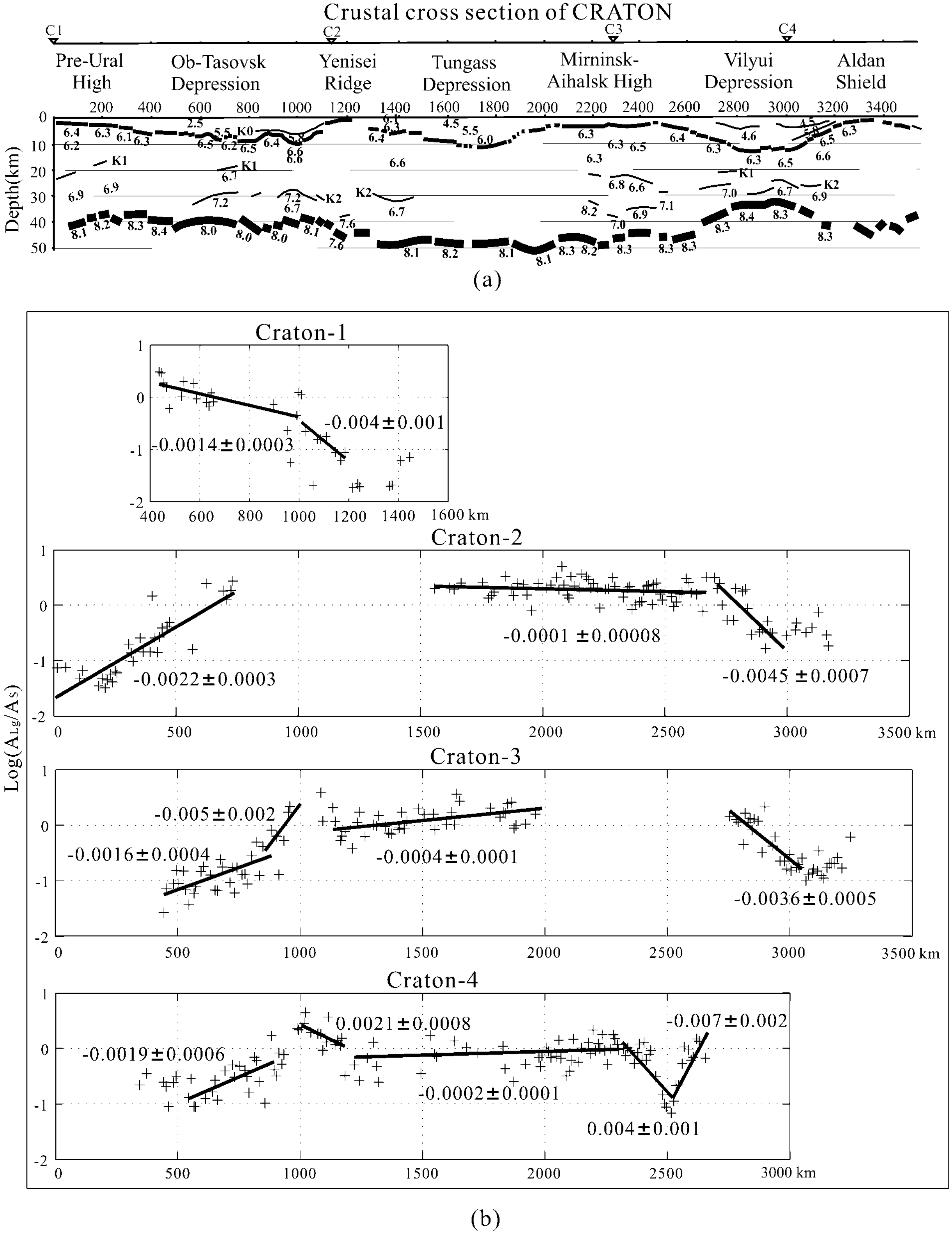

Figure 4. (a) Crustal cross section along the Craton profile (Egorkin *et al.*, 1987), (b) $\log(A_{Lg}/A_{Sn})$, and (c) $\log(A_{Lg}/A_{Pcoda})$ vector amplitude ratios from Craton-1, Craton-2, Craton-3, and Craton-4. Three basins along the profile are the Ob-Tasovsk Depression, Tunguss Depression, and Vilyui Depression. The slopes of both ratios are ~ -0.0018 km^{-1} in the Ob-Tasovsk Depression; ~ -0.005 km^{-1} across the Yenisei Ridge; ~0 in the Tunguss Depression and the Mirninsk-Aihalsk High; and ~ -0.0045 km^{-1} in the Vilyui Depression. *(continued)*

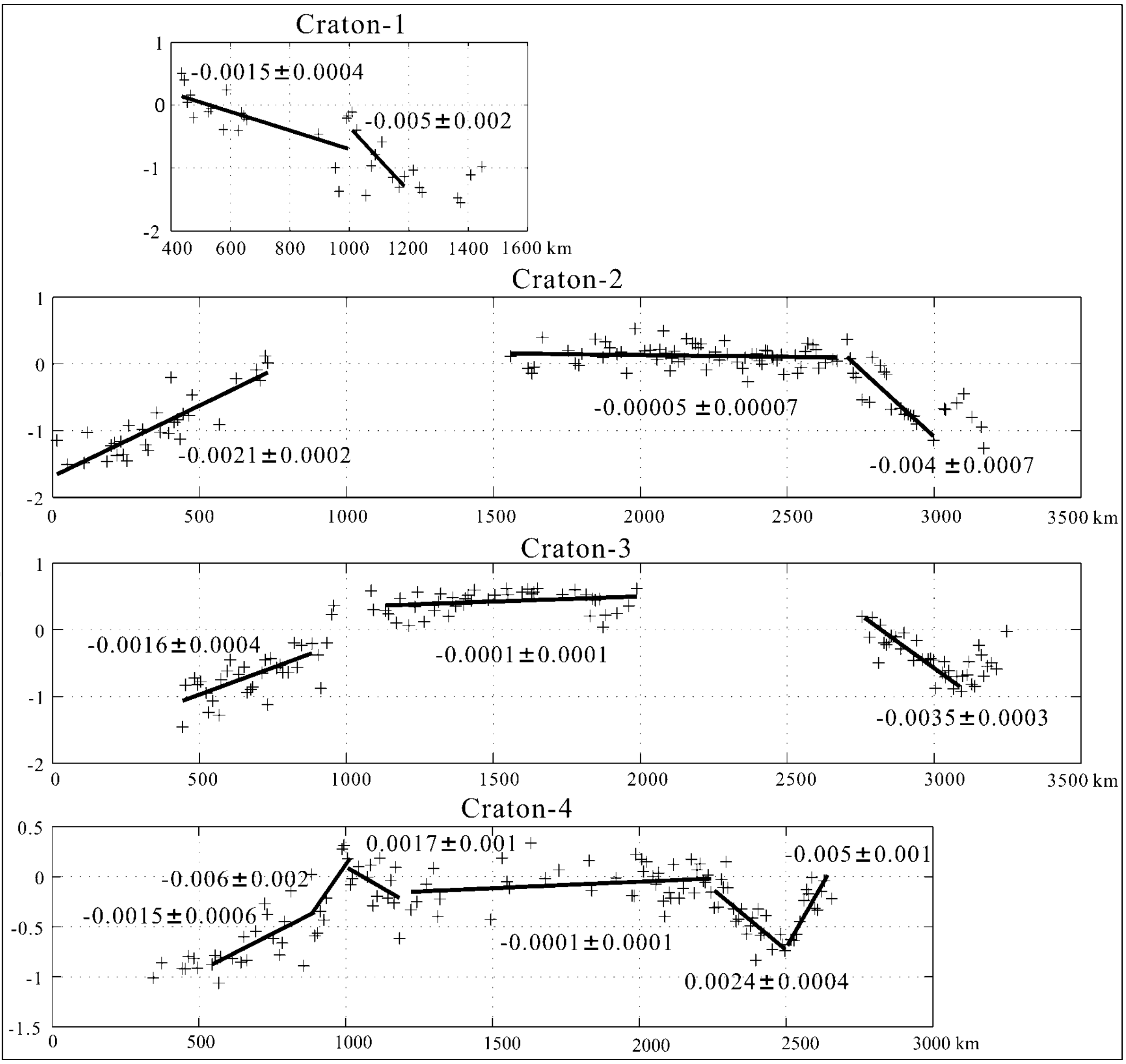

(c)

Figure 4. Continued.

parison of the slopes across the West Siberian Basin and the Tunguss Basin (Fig. 4) demonstrated that the slopes of both ratios are not only related to the thickness of the sedimentary cover, but also the velocity.

The slopes of both log(A_{Lg}/A_{Sn}) and log(A_{Lg}/A_{Pcoda}) of different segments along all the seven PNE profiles with the corresponding Moho slope, the velocity (V_P and V_S) and thickness of the sedimentary cover (Table 1) show that the slopes of both ratios are close for all the segments along all the seven profiles of this study. Larger slopes (≤ -0.003 km^{-1}) are found within the Vilyui Depression, the Ural Mountains, across the Yenisei Ridge, the boundary between the Kazakh massif and the West Siberian Basin, and the Mezen Depression. All these locations correspond to abrupt crustal thinning or thickening. Moderate slopes ($-0.001 \sim -0.003$ km^{-1}) correspond to thick low-velocity sedimentary cover and/or moderate crustal variations in the West Siberian Basin, the Angara-Lena Terrace, and the southern part of the Siberian Craton. Low slopes (> -0.001 km^{-1}) correspond to cratons with thin sedimentary cover (the Siberian Craton, the East European Craton, and the Kazakh massif) or in sedimentary basins with thin (the Timan-Pechora Basin) or thick but high-velocity (the Tunguss Basin and the Low Angara Basin) sedimentary cover and small Moho variations. The shear velocity of the sedimentary basins is determined by comparing the *P*-wave velocity from the available velocity profiles and the global Crustal Model CRUST 2.0 for V_P, V_S, density, and thickness of all the crustal layers (Bassin *et al.*, 2000).

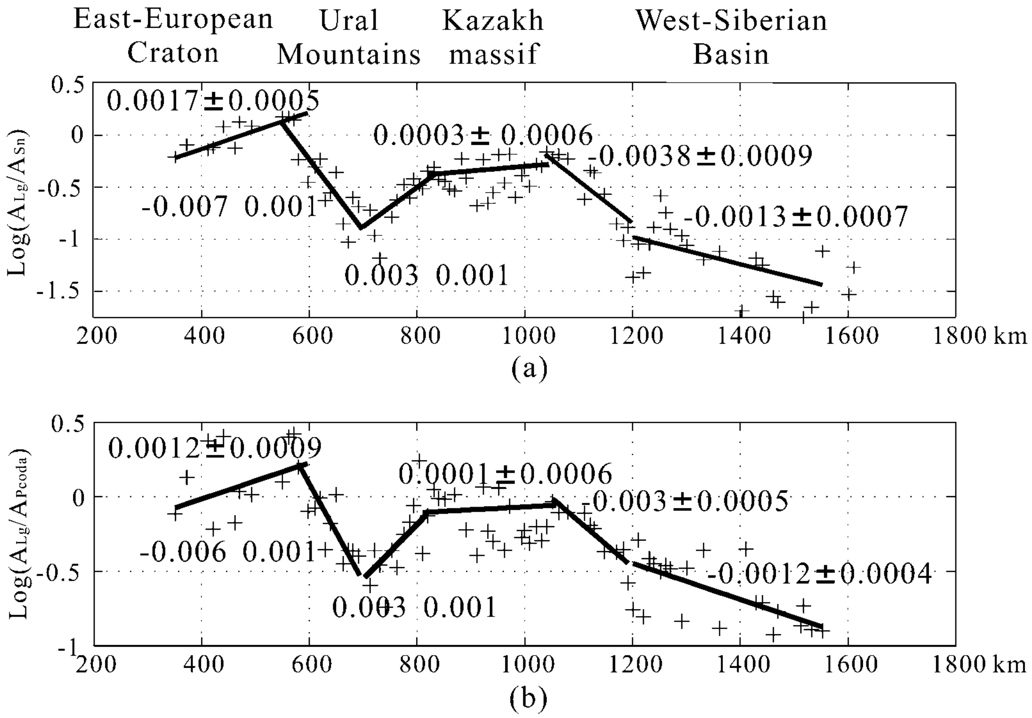

Figure 5. Log(A_{Lg}/A_{Sn}) (a) and log(A_{Lg}/A_{Pcoda}) (b) vector amplitude ratios from Ruby-1. The slope of both ratios is -0.006 to -0.007 km^{-1} across the Ural Mountains followed by a ~0.003 km^{-1} positive slope at further offsets. The slope is quite flat in the Kazakh massif followed by a strong negative slope (-0.003 to -0.004 km^{-1}) across the boundary toward the West Siberian Basin and a smaller negative slope (-0.0012 to -0.0013 km^{-1}) in the West Siberian Basin.

Discussion

From the amplitude ratios of log(A_{Lg}/A_{Sn}) and log(A_{Lg}/A_{Pcoda}) within different frequency bands (Fig. 3), it is apparent that the energy of the *Lg* phase is mainly concentrated at lower frequencies, similar to the observations by Gupta *et al.* (1992). Moreover, the slope of both amplitude ratios within the low-frequency bands correlates much more clearly with the variations of crustal structure than does the high-frequency band (4–8 Hz), because the *Lg* phase in mainly concentrated at low frequencies. Along the seven PNE profiles, the range of variation (Fig. 3), the general trend (Fig. 3), and the slopes (Table 1) of both log(A_{Lg}/A_{Sn}) and log(A_{Lg}/A_{Pcoda}) are always close to each other, especially at low frequencies. This article used both ratios within a low-frequency band (0.5–3 Hz) to study *Lg* propagation to improve data reliability.

In this study, a constant time window is used for *Lg, Sn*, and *Pcoda* due to limited data length of some traces. By calculating the logarithm of *Lg*-amplitude ratios of constant amplitude window (20 sec) over velocity window (3.6–3.0 km/sec), the slope of the ratios varies from 0 to 0.0003 km^{-1}, hardly related to the variations of crustal structure. Therefore, the selection of time window does not affect the slope of the logarithms of amplitude ratios.

According to the slopes of log(A_{Lg}/A_{Sn}) and log(A_{Lg}/A_{Pcoda}) from all the 19 PNE seismic records along the seven profiles in northern Eurasia (Table 1), the slopes of both amplitude ratios in different tectonic areas are summarized in Figure 6. The large slopes (< -0.003 km^{-1}) are located in the Vilyui Depression, across the Ural Mountains and the boundary between the West Siberian Basin and the Siberian Craton, corresponding to the abrupt variations of crustal thickness. The flat slopes are determined in the East European Craton, the Kazakh massif, and the Siberian Craton with thin sedimentary cover and gentle variations of Moho depth. The slope is ~ -0.001 to -0.002 km^{-1} in the West Siberian Basin with thick, low-velocity sedimentary cover and gently varying Moho.

The slopes of both log(A_{Lg}/A_{Sn}) and log(A_{Lg}/A_{Pcoda}) decrease with the increase of Moho dip (dH_M/dx) and the increase of the travel time (H_S/V_{SS}, the thickness of the sedimentary cover H_S divided by the shear velocity V_{SS}, Bassin *et al.*, 2000) through the sedimentary cover (Fig. 7). According to Zhang *et al.* (1994) and Fan and Lay (1998a, b), the variation of the Moho depth and the thickness of the sedimentary basin are two main factors that affect *Lg* propagation. The linear relationship of the slopes of both amplitude ratios with the Moho slope and the vertical travel time through the sedimentary cover (Fig. 7) demonstrated that the Moho slope is the main factor that affects *Lg* propagation in

Table 1

The Slope of $\log(A_{Lg}/A_{Sn})$ and $\log(A_{Lg}/A_{Pcoda})$, the Corresponding Average Moho Slope, and the Corresponding Average Vertical Travel Time through the Sedimentary Cover from All the PNEs along Different Segments

Profile*	Location	Segment Length x (km)	$\frac{d(\log(A_{Lg}/A_{Sn})}{dx} \times 10^{-3}$	$\frac{d(\log(A_{Lg}/A_{Pcoda})}{dx} \times 10^{-3}$	Moho: Δ Moho H_M (km)	Moho: $d(H_M)/dx \times 10^{-3}$	Sedimentary Cover†: V_{PS} (km/sec)	Sedimentary Cover†: V_{SS} (km/sec)	Sedimentary Cover†: Thickness H_S (km)	Sedimentary Cover†: H_S/V_{SS}
CRATON	West Siberian Rift	600	−1.8 ± 0.4	1.7 ± 0.4	−5	−6	3.8	1.9	7	3.7
	Yenisei Ridge	200	−4 ± 1	−5 ± 2	10	50	3.7	1.9	4	2.1
	Yenisei Ridge	200	−5 ± 2	−6 ± 2	−10	−50	3.7	1.9	4	2.1
	Tunguss Basin	600	−0.3 ± 0.1	−0.1 ± 0.1	0	0	6.2	3.6	7	1.9
	Siberian Craton	600	−0.1 ± 0.1	−0.08 ± 0.07	−4	−7	6	3.5	3	0.9
	Vilyui Depression	300	−7 ± 2	−5 ± 1	13	43	4.1	2.6	8	3.1
	Vilyui Depression	300	−4 ± 0.5	−3.8 ± 0.5	−13	−43	4.1	2.6	8	3.1
KIMBERLITE	West Siberian Basin	300	−4.7 ± 0.8	−4.5 ± 0.7	−8	−27	3.8	1.9	6	3.2
	Tunguss Basin	800	−0.6 ± 0.08	−0.5 ± 0.06	−5	−6	5.5	3.2	6	1.9
	Siberian Craton	800	−0.4 ± 0.2	−0.2 ± 0.2	0	0	5.5	3.2	3	0.9
	Vilyui Depression	200	−5.1 ± 0.8	−3.9 ± 0.8	−10	−50	4.1	2.6	7	2.7
METEORITE	Siberian Craton	400	−1.5 ± 0.2	−1.1 ± 0.2	−5	−13	5.5	3.2	7	2.2
	Siberian Craton	400	0.1 ± 0.2	0.1 ± 0.2	0	0	5.2	3.0	4	1.3
	Angara-Lena Terrace	400	−1.4 ± 0.4	−1.2 ± 0.3	−6	−15	5.2	3.0	3	1.0
QUARTZ	Baltic Shield	700	−0.6 ± 0.3	−0.4 ± 0.3	5	7	6	3.5	0	0
	Mezen Depression	200	−4 ± 1.5	−3 ± 1	−6	−30	3.6	1.8	3	1.7
	Timan Belt & Timan-Pechora Basin	500	−0.9 ± 0.1	−0.8 ± 0.1	2	4	3.3	1.7	2	1.2
	West Siberian Basin	1300	−1.5 ± 0.3	−1.4 ± 0.3	5	4	3.8	1.9	6	3.2
RIFT	Yenisei Ridge	300	−0.3 ± 0.5	−0.4 ± 0.4	0	0	6	3.5	1	0.17
	Tunguss Basin, Low Angara Basin	1400	−1 ± 0.1	−0.9 ± 0.1	10	−7	6	3.5	6	1.7
RUBY-1	East European Craton	250	1.7 ± 0.5	1.2 ± 0.8	0	0	6	3.5	1	0.28
	Ural Mountains	150	−7 ± 1	−6 ± 1	14	90	3.3	1.7	2	1.2
	Ural Mountains	150	4 ± 1	3 ± 1	−14	90	3.3	1.7	2	1.2
	Kazakh massif	350	0.3 ± 0.6	0.1 ± 0.5	0	0	6	3.5	1	0.28
	West Siberian Basin	100	−3.8 ± 0.9	−3.1 ± 0.5	−7	−70	3.8	1.8	2	1.1
	West Siberian Basin	550	−1.3 ± 0.7	−1.2 ± 0.4	3	5	3.6	1.8	4	2.2
RUBY-2	West Siberian Basin	700	−1.4 ± 0.2	−1.4 ± 0.2	6	9	3.9	2.0	5	2.5

* The crustal structure along different profiles are from: CRATON, Egorkin *et al.*, 1987; KIMBERLITE, Pavlenkova, 1996; METEORITE, Elena Morozova, personal communication with GEON in Russia; QUARTZ, Beloussov *et al.*, 1992a, b, and Morozova *et al.*, 1999; RIFT, Pavelenkova *et al.*, 2002; RUBY-1 and RUBY-2, constructed from the basement map and crustal thickness map provided by Aplonov, 1995, and Pavlenkova, 1996.

† V_{PS} and V_{SS} are separately the average *P*- and *S*-wave velocity of the sedimentary cover.

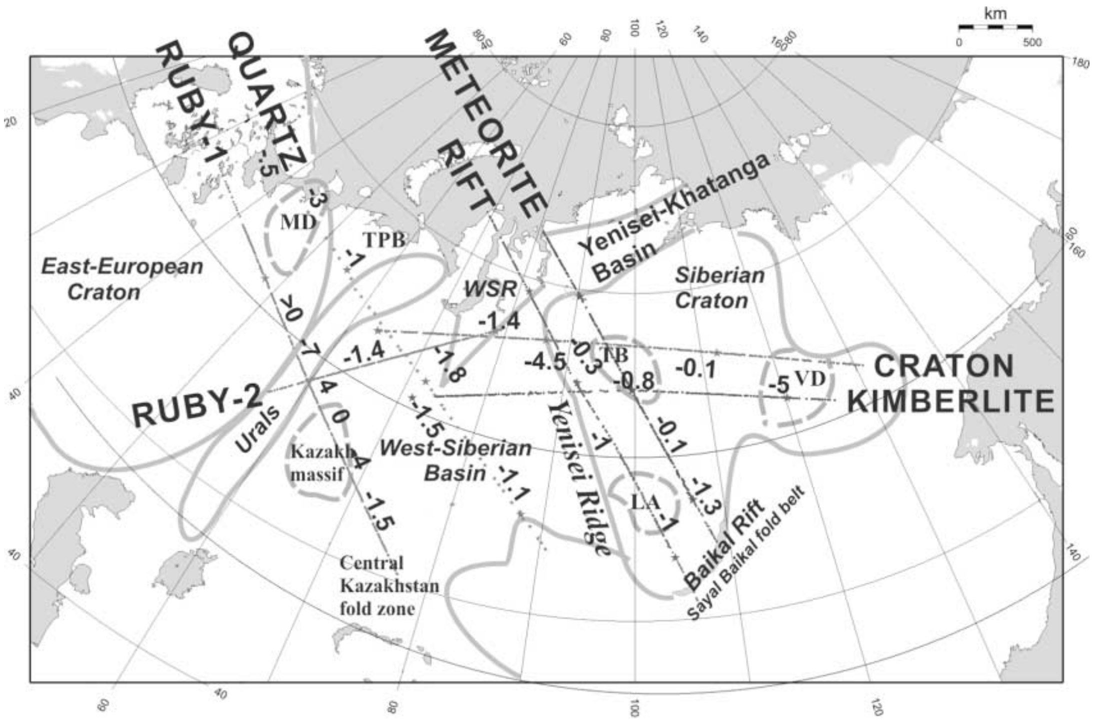

Figure 6. Sketch of tectonic boundaries in northern Eurasia. Labels indicate the residual slopes of the log-amplitude ratios in different tectonic areas observed from the seven PNE profiles, in units of 0.001 km^{-1}. WSR, West Siberian Rift; TB, Tunguss Basin; LA, Low Angara Depression; VD, Vilyui Depression; MD, Mezen Depression.

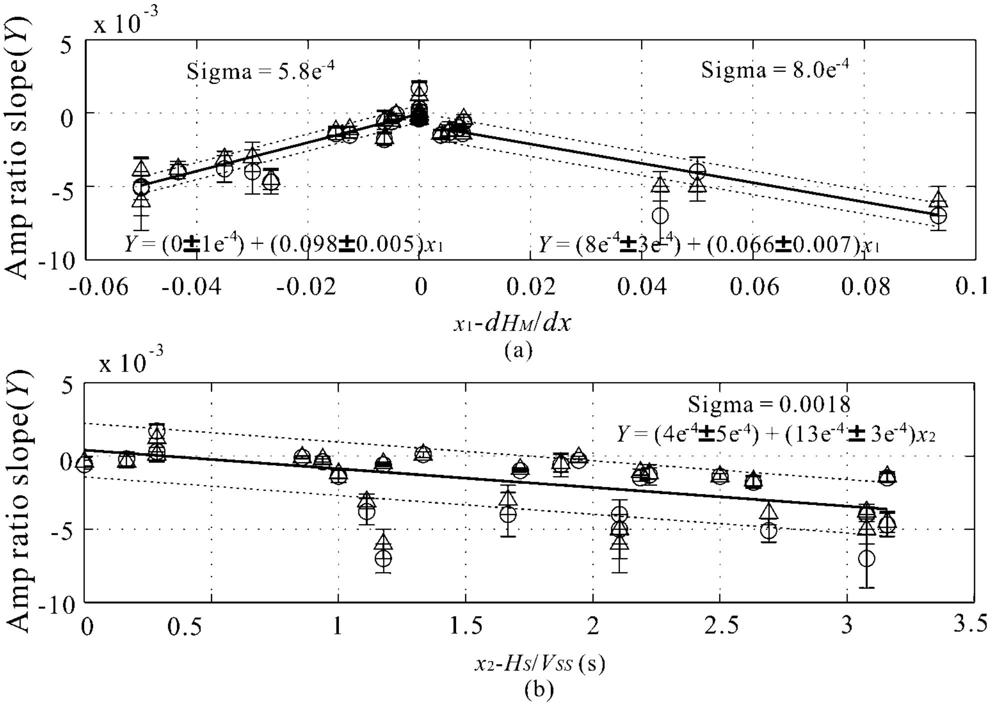

Figure 7. The linear relationship (solid lines) of the slopes of log(*Lg*/*Sn*) and log(*Lg*/*Pcoda*) (Y) with dH_M/dx (x_1, a) and with H_S/V_{SS} (x_2, b). The slopes of log(*Lg*/*Sn*) (O) are close to those of log(*Lg*/*Pcoda*) (Δ) and the error bars are also shown. The standard error (dashed lines) and the slope error of (a) are much smaller than (b).

northern Eurasia. The effect of thick sedimentary rocks on *Lg* propagation depends on the velocity.

One linear relationship is simultaneously determined for the slopes of both amplitude ratios, as a function of the corresponding dH_M/dx and H_S/V_{SS}. The selection of these parameters is dictated by a conjecture that the two most significant crustal parameters should be the corresponding Moho depth gradient (responsible for local focusing/defocusing of *Lg* waves) and the average *S*-wave travel time through a sedimentary cover (primarily responsible for attenuation).

Considering only the areas of crustal thinning (Table 1), the best-fit regression for the slopes of log-amplitude ratios becomes:

$$\frac{d\ \log(A_{Lg}/A_{Ph})}{dx} = 5 \cdot 10^{-4} + 8.0 \cdot 10^{-2} \cdot \frac{dH_M}{dx} - 6 \cdot 10^{-4}\,\frac{H_S}{V_{SS}}, \qquad (10)$$

and in the areas of crustal thickening:

$$\frac{d\ \log(A_{Lg}/A_{Ph})}{dx} = 5 \cdot 10^{-4} - 7.5 \cdot 10^{-2} \cdot \frac{dH_M}{dx} - 6 \cdot 10^{-4}\,\frac{H_S}{V_{SS}}. \qquad (11)$$

Because the regression coefficients for the crustal thinning and thickening are close, a common linear regression was also determined:

$$\frac{d\ \log(A_{Lg}/A_{Ph})}{dx} = 5 \cdot 10^{-4} - 7.7 \cdot 10^{-2} \cdot \left|\frac{d(H_M)}{d(x)}\right| - 6 \cdot 10^{-4}\,\frac{H_S}{V_{SS}}. \qquad (12)$$

with an estimated error of $6.8 \cdot 10^{-4}$.

Across the Vilyui Depression (Fig. 4), the Yenisei Ridge (Fig. 4), and the Ural Mountains (Fig. 5), a strong negative slope is observed across both abrupt crustal thinning and crustal thickening segments. However, the negative slope appears at farther offsets across the crustal thinning ramp than the crustal thickening ramp. Moreover, the negative slope is followed by a positive slope along the crustal thickening direction, i.e., the *Lg* energy partially recovers after crustal thickening. Therefore, crustal thickening is observed to affect *Lg* propagation, in general, less significantly than crustal thinning. The effective slope of both ratios across the Vilyui Depression in the crustal thickening direction is $\sim -0.006 + 0.003 = -0.003\ \text{km}^{-1}$; the effective slope across the Ural Mountains is $\sim -0.007 + 0.004 = -0.003\ \text{km}^{-1}$. These observations of the different effects of crustal thinning and crustal thickening on *Lg* propagation should be addressed in further study.

To explain the difference of *Lg*-propagation characteristics in opposite directions across the same structure, consider two crustal models (Fig. 8; Regan and Harkrider, 1989; Cao and Murihead, 1993). For crustal thickening, the *Lg* energy, and therefore the A_{Lg}/A_{Sn} and A_{Lg}/A_{Pcoda} amplitude ratios, decreases within the crustal thickening segment, which could be due to defocusing, and then increases after the crustal thickening segment due to focusing. Therefore, a negative slope followed by a positive slope is observed across a crustal thickening segment. For crustal thinning, the *Lg* energy drops quickly at farther offsets within a thin crust because a larger number of reflections are involved in formation of the *Lg*, as a result of which the energy could leak into the mantle (Regan and Harkrider, 1989; Wu *et al.*, 2000a, b) or become backscattered into the opposite direction (Cao and Muirhead, 1993). *Lg* energy may increase along the crustal thinning ramp, which could be due to focusing and the backscattered *Lg* energy (Regan and Harkrider, 1989; Cao and Muirhead, 1993). Therefore, a negative slope is usually observed at farther offsets across a crustal thinning segment. Modeling of *Lg* propagation across a crustal antiroot and a crustal root (Wu *et al.*, 2000a, b) supported that a crustal antiroot affects the *Lg* propagation stronger than a crustal root (Fig. 8). In the latter case, although the wavefronts are also complicated due to scattering at the edges, more energy is trapped in the crust than the case of crustal antiroot in which a large percentage of *Lg* energy leaks into the mantle.

The effect of sedimentary basins can be associated with both intrinsic and scattering attenuation. Without considering geometrical spreading, equation (1) can be described as

$$A_{Lg2} = A_{Lg1}e^{-\eta_{Lg}(x_2-x_1)} = A_{Lg1}e^{-(\eta_S H_S/H_M+\eta_C H_C/H_M)(x_2-x_1)}, \qquad (13)$$

where η_{Lg} is the *Lg* attenuation coefficient through the whole crust, H_C and η_C are the thickness and attenuation coefficient of the crystalline crust, η_S is the attenuation coefficient of the sedimentary basin. Because η_C is much smaller than η_S, equation (13) can be simplified as

$$A_{Lg2} = A_{Lg1}e^{\eta_S H_S/H_M(x_2-x_1)} \approx A_{Lg1}e^{-n'_S H_S(x_2-x_1)}. \qquad (14)$$

Because high (low) attenuation corresponds to low (high) velocity, H_S/V_{SS} is used to describe the effect of sedimentary basins on *Lg* propagation.

Conclusions

In northern Eurasia, the slopes of the logarithms of *Lg*/*Sn* and *Lg*/*Pcoda* amplitude ratios at frequencies of 0.5–3 Hz could be useful parameters to calibrate the effects of the variations in the crustal structure on *Lg* propagation. Records from seven ultralong profiles sourced by 19 PNEs were used to correlate these slopes with the crustal structures. After

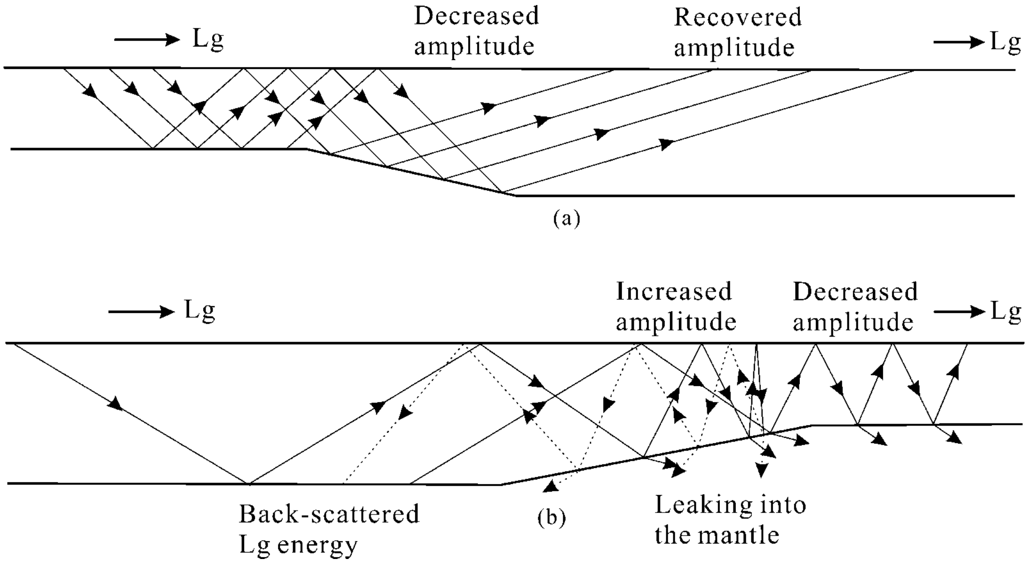

Figure 8. Comparison of the effects of (a) crustal thickening and (b) crustal thinning on *Lg* propagation based on a ray-summation model. Across a crustal thickening segment, the *Lg* amplitude is expected to drop abruptly at the crust-thickening ramp due to defocusing, but the amplitude will partially recover after passing the segment. Across a crustal thinning segment, the *Lg* amplitude increases at the upward Moho ramp due to ray focusing but drops quickly at farther offsets in the thin crust because of *Lg* energy leaking into the mantle or being backscattered (Regan and Harkrider, 1989).

removing the average offset trend measured for travel paths within the Siberian Craton, the slope of both ratios is positive or flat in cratonic areas with thin sedimentary cover and small Moho variations. The slope is negative within sedimentary basins and near tectonic boundaries with abrupt variations of crustal thickness. A linear relation of the slopes of both logarithms of amplitude ratios to the corresponding Moho slope $d(H_M)/d(x)$ and the average vertical travel time of *Lg* through the sedimentary cover (H_S/V_{SS}) was obtained:

$$\frac{d\,\log(A_{Lg}/A_{Ph})}{dx} = 5\cdot 10^{-4} - k\cdot\left|\frac{dH_M}{dx}\right| - 6\cdot 10^{-4}\,\frac{H_S}{V_{SS}},$$

with an estimated error of $6.8\cdot 10^{-4}$. Where the regression parameter $k \approx 8\cdot 10^{-2}$ in the areas of crustal thinning and $k \approx 7.5\cdot 10^{-2}$ for crustal thickening. Strong negative slopes were identified across the Ural Mountains, the Vilyui Depression, the Yenisei Ridge, the boundary between the Kazakh massif and the West Siberian Basin, and within the Mezen Depression. Although the propagation parameter *k* is similar for crustal thinning and crustal thickening, a positive slope follows the strong negative slope along the crustal thickening direction, that is, the *Lg* energy partially recovers at further offsets. Overall, from the PNE data, the abrupt variation of crustal thickness, and in particular, crustal thinning, is the most important factor affecting *Lg*-phase propagation and *Lg*-based seismic discriminants.

References

Aplonov, S. V. (1995). The tectonic evolution of West Siberia: an attempt at a geophysical analysis, *Tectonophysics* **245,** 61–84.

Bassin, C., G. Laske, and G. Masters (2000). The current limits of resolution for surface wave tomography in North America, *EOS Trans. AGU* **81,** F897.

Baumgardt, D. R. (2001). Sedimentary basins and the blockage of *Lg* wave propagation in the continents, *Pure Appl. Geophys.* **158,** 1207–1250.

Beloussov, V. V., N. I. Pavlenkova, and G. N. Kvyatkovskaya (1992a). Structure of the crust and upper mantle of the [Former] USSR. Part I, Integrated geophysical models of the major geostructures of the USSR, *Int. Geol. Rev.* **34,** 213–343.

Beloussov, V. V., N. I. Pavlenkova, and G. N. Kvyatkovskaya (1992b). Structure of the crust and upper mantle of the [Former] USSR. Part II, Generalized geophysical data on the structure of the tectonosphere of the USSR, *Int. Geol. Rev.* **34,** 345–444.

Campillo, M. (1987). *Lg* wave propagation in a laterally varying crust and the distribution of the apparent quality factor in central France, *J. Geophys. Res.* **92,** 12,604–12,614.

Cao, S., and K. J. Muirhead (1993). Finite difference modeling of *Lg* blockage, *Geophys. J. Int.* **115,** 85–96.

Carbonell, R., S. Kashubin, J. Mechie, R. Stadtlander, A. Schulze, J. H. Knapp, A. Morozov, A. Perez-Estaun, J. Gallart, and J. Diaz (1996). Crustal root beneath the Urals: wide-angle seismic evidence, *Science* **274,** 222–224.

Cipar, J. J., K. Priestley, A. V. Egorkin, and N. I. Pavlenkova (1993). The Yamal Peninsula-Lake Baikal deep seismic sounding profile, *Geophys. Res. Lett.* **20,** 1631–1634.

Czamanske, G. K., A. B. Gurevich, V. Fedorenko, and O. Simonov (1998). Demise of the Siberian plume: paleogeographic and paleotectonic reconstruction from the prevolcanic and volcanic records, North-Central Siberia, *Int. Geol. Rev.* **40,** 95–115.

Dehandschutter, B. (2001). Study of the recent structural evolution of continental basins in Altay-Sayan, http://users.pandora.be/boris.dehandschutter/chapter-1.PDF (last accessed October 2005).

Egorkin, A. V., S. K. Zuganov, N. A. Pavlenkova, and N. M. Chernyshev (1987). Results of lithospheric studies from long-range profiles in Siberia, *Tectonophysics* **140,** 29–47.

Fan, G., and T. Lay (1998a). Statistical analysis of irregular wave-guide influence on regional seismic discriminants in China, *Bull. Seism. Soc. Am.* **88,** 74–88.

Fan, G., and T. Lay (1998b). Statistical analysis of irregular wave-guide influence on regional seismic discriminants in China: additional results for *Pn*/*Sn, Pn*/*Lg*, and *Pg*/*Sn*, *Bull. Seism. Soc. Am.* **88,** 1504–1510.

Gaal, G., and R. Gorbatschev (1987). An outline of the Precambrian evolution of the Baltic shield, *Precam. Res.* **35,** 15–52.

Golmshtok, A. Y., A. D. Duchkov, D. R. Hutchinson, and S. B. Khanukaev (2000). Heat flow and gas hydrates of the Baikal Rift zone, *Int. J. Earth Sci.* **89,** 193–211.

Gupta, I. N., W. W. Chan, and R. A. Wagner (1992). A comparison of regional phases from underground nuclear explosions at east Kazakh and Nevada test sites, *Bull. Seism. Soc. Am.* **82,** 352–382.

Gupta, I. N., T. R. Zhang, and R. A. Wagner (1997). Low-frequency *Lg* from NTS and Kazakh nuclear explosions—observations and interpretation, *Bull. Seism. Soc. Am.* **87,** 1115–1125.

He, Y.-F., X.-F. Chen, and H.-M. Zhang (2005). The excitation of *Lg* wave by underground nuclear explosions, *Chin. J. Geophys.* **48,** 367–372.

Hutchinson, D. R., A. J. Golmshtok, L. P. Zonenshain, T. C. Moore, C. A. Scholz, and K. D. Klitgord (1992). Depositional and tectonic framework of the rift basins of Lake Baikal from multichannel seismic data, *Geology* **20,** 589–592.

Kennett, B.L.N. (1993). The distance dependence of regional phase discriminants, *Bull. Seism. Soc. Am.* **83,** 1155–1166.

Khain, V. E. (1985). *Geology of the USSR*, Part 1, Gebrüder Borntraeger, Berlin.

Khain, V. E. (1994). *Geology of northern Eurasia (ex-USSR)*, Part 2, Gebrüder Borntraeger, Berlin.

Knopoff, L., F. Schwab, and E. Kausel (1973). Interpretation of *Lg*, *Geophys. J. R. Astr. Soc.* **33,** 389–404.

Logatchev, N. A., and Yu. A. Zorin (1992). Baikal Rift zone: structure and geodynamics, *Tectonophysics* **208,** 273–286.

McNamara, D. E., and W. R. Walter (2001). Mapping crustal heterogeneity using *Lg* propagation efficiency throughout the Middle East, Mediterranean, Southern Europe, *Pure Appl. Geophys.* **158,** 1165–1188.

Morozov, I. B. (2001). Comment on "High-frequency wave propagation in the uppermost mantle" by T. Ryberg and F. Wenzel, *J. Geophys. Res.* **106,** 30,715–30,718.

Morozov, I. B., S. B. Smithson, and L. N. Solodilov (2002). Imaging crustal structure along refraction profiles using multicomponent recordings of first-arrival coda, *Bull. Seism. Soc. Am.* **92,** 3080–3086.

Morozova, E. A., I. B. Morozov, S. B. Smithson, and L. Solodilov (1999). Heterogeneity of the uppermost mantle beneath Russian Eurasia from the ultra-long-range profile QUARTZ, *J. Geophys. Res.* **104,** 20,329–20,348.

Nielsen, L., and T. Thybo (2003). The origin of teleseismic *Pn* waves: multiple crustal scattering of upper mantle whispering gallery phases, *J. Geophys. Res.* **108,** 2460, doi 10.1029/2003JB002487.

Pavlenkova, N. I. (1996). Crust and upper mantle structure in northern Eurasia from seismic data, *Adv. Geophys.* **37,** 1–133.

Pavlenkova, G. A., K. Priestley, and J. Ciper (2002). 2D model of the crust and uppermost mantle along Rift profile, Siberian Craton, *Tectonophysics* **355,** 171–186.

Phillips, W. S., H. E. Hartse, S. R. Taylor, A. A. Velasco, and G. E. Randall (2001). Application of regional phase amplitude tomography to seismic verification, *Pure Appl. Geophys.* **158,** 1189–1206.

Rapine, R. R., and J. F. Ni (2003). Propagation characteristics of *Sn* and *Lg* in Northern China and Mongolia, *Bull. Seism. Soc. Am.* **93,** 939–945.

Rapine, R. R., J. F. Ni, and T. M. Hearn (1997). Regional wave propagation in China and its surrounding regions, *Bull. Seism. Soc. Am.* **87,** 1622–1636.

Regan, J., and D. G. Harkrider (1989). Numerical modelling of SH *Lg* waves in and near continental margins, *Geophys. J. Int.* **98,** 107–130.

Ryberg, T., K. Fuchs, A.V. Egorkin, and L. Solodilov (1995). Observation of high-frequency teleseismic *Pn* on the long-range Quartz profile across northern Eurasia, *J. Geophys. Res.* **100,** 18,151–18,163.

Sandvol, E., K. Al-Damegh, A. Calvert, D. Seber, M. Barazangi, R. Mohamad, R. Gök, N. Türkelli, and C. Gürbüz (2001). Tomographic imaging of *Lg* and *Sn* propagation in the Middle East, *Pure Appl. Geophys.* **158,** 1121–163.

Saunders, A. D., R. V. White, R. W. England, and M. K. Reichow (2005). A mantle plume origin for the Siberian traps: Uplift and extension in the West Siberian Basin, Russia, *Lithos* **79,** 407–424.

Tryggvason, A., D. Brown, and A. Perez-Estaun (2001). Crustal structure of the southern Uralides from true amplitude processing of the Urals Seismic Experiment and Integrated Studies (URSEIS) vibroseis profile, *Tectonics* **20,** 1040–1052.

Ulmishek, G. F. (2003). Petroleum geology and resources of the West-Siberian Basin, Russia, *U.S. Geol. Surv. Bull. 2201-G*.

Volkov, V. M. (1984). Geology of the USSR: Colloquium 01, in *27th International Geological Congress*, USSR, Moscow, 4–14 August, 1984. Publishing Office "Nauka," Moscow.

Wu, R. S., S. Jin, and X. B. Xie (2000a). Seismic wave propagation and scattering in heterogeneous crustal waveguide using screen propagators: I SH waves, *Bull. Seism. Soc. Am.* **90,** 401–413.

Wu, R. S., S. Jin, and X. B. Xie (2000b). Energy partition and attenuation simulations using screen propagators, *Phys. Earth Planet. Interiors* **120,** 227–243.

Zhang, T.-R., S. Y. Schwartz, and T. Lay (1994). Multivariate analysis of waveguide effects on short-period regional wave propagation in Eurasia and its application in seismic discrimination, *J. Geophys. Res.* **99,** 21,929–21,945.

Zonenshain, L. P., M. I. Kuzmin, and B. M. Natapov (1990). *Geology of the USSR: A Plate Tectonic Synthesis*, American Geophysical Union, Washington, D.C.

Zorin, Yu. A., E. Kh. Turutanov, V. V. Mordvinova, V. M. Kozhevnikov, T. B. Yanovskaya, and A. V. Treussov (2003). The Baikal rift zone: the effect of mantle plumes on older structure, *Tectonophysics* **371,** 153–173.

Department of Geology and Geophysics
University of Wyoming
Laramie, Wyoming 82071-3006
snow@uwyo.edu
lhysnow@yahoo.com
sbs@uwyo.edu
(H.L., I.B.M., S.B.S.)

University of Saskatchewan
114 Science Place
Saskatoon, Saskatchewan S7N5E2, Canada
igor.morozov@usask.ca
(I.B.M.)

Manuscript received 17 May 2006.